Applied Mathematical Modelling 35 (2011) 4157–4174

Contents lists available at ScienceDirect

Applied Mathematical Modelling

journal homepage: www.elsevier.com/locate/apm

Nonlinear transient heat conduction analysis of functionally graded materials in the presence of heat sources using an improved meshless radial point interpolation method

A. Khosravifard [a], M.R. Hematiyan [a], L. Marin [b,c,*]

[a] Department of Mechanical Engineering, Shiraz University, Shiraz 71345, Iran
[b] Institute of Solid Mechanics, Romanian Academy, 010141 Bucharest, Romania
[c] Centre for Continuum Mechanics, Faculty of Mathematics and Computer Science, University of Bucharest, 010014 Bucharest, Romania

ARTICLE INFO

Article history:
Received 5 August 2010
Received in revised form 7 February 2011
Accepted 18 February 2011
Available online 23 February 2011

Keywords:
Nonlinear
Transient heat conduction
Meshless radial point interpolation method (RPIM)
Functionally graded materials (FGMs)
Meshless integration

ABSTRACT

An improved meshless radial point interpolation method, for the analysis of nonlinear transient heat conduction problems is proposed. This method is implemented for the heat conduction analysis of functionally graded materials (FGMs) with non-homogenous and/or temperature dependent heat sources. The conventional meshless RPIM is an appropriate numerical technique for the analysis of engineering problems. One advantage of this method is that it is based on the global weak formulation, and also the associated shape functions possess the Kronecker delta function property. However, in the original form, the evaluation of the global domain integrals requires the use of a background mesh. The proposed method benefits from a meshless integration technique, which has the capability of evaluating domain integrals with a better accuracy and speed in comparison with the conventional integration methods, and therefore a truly meshless technique is attained. This integration technique is especially designed for the fast and accurate evaluation of several domain integrals, with different integrands, over a single domain. Some 2D and 3D examples are provided to assess the efficiency of the proposed method.

1. Introduction

Transient heat transfer is an important phenomenon that occurs in many engineering problems. Since temperature varies with respect to time in many industrial parts, the precise knowledge of the temperature distribution and variation in such parts is essential. It is well known that analytical solutions can be found for simple geometries and linear heat transfer problems only. However, in most practical situations, not only the geometry of the part under investigation is complicated, but also the material has temperature dependent thermal properties. Moreover, the heat generation in the domain might be dependent on the temperature. When dealing with such practical situations, the only possibility for obtaining reasonable results is the use of appropriate numerical methods.

Functionally graded materials (FGMs) are composite materials where, in contrast to the laminated composites, the composition of the constituent materials gradually varies so that a certain variation of the material properties is achieved. These materials have received considerable attention since their concept was proposed in the late 1980s in Japan. FGMs are made

---

* Corresponding author. Address: Institute of Solid Mechanics, Romanian Academy, 15 Constantin Mille, P.O. Box 1-683, 010141 Bucharest, Romania. Tel./fax: +40 21 3126736.

E-mail addresses: khosravifard@shirazu.ac.ir (A. Khosravifard), mhemat@shirazu.ac.ir (M.R. Hematiyan), marin.liviu@gmail.com, liviu@imsar.bu.edu.ro (L. Marin).

0307-904X/$ - see front matter © 2011 Elsevier Inc. All rights reserved.
doi:10.1016/j.apm.2011.02.039

to exploit the desirable properties of their individual constituents. Typically, FGMs are made of a mixture of two materials, namely ceramics and metals. The former are capable of withstanding high temperature environments due to their low thermal conductivity and provide corrosion resistance, while the latter, by their good mechanical properties, strengthen the structure to support loadings or prevent material failure.

The finite element method (FEM) is a well established tool for analyzing non-homogenous and non-linear problems in engineering. Nevertheless, there are some intrinsic shortcomings associated with the finite elements that limit the application of the method to some particular situations. To mention some, large deformation processes, dynamic crack propagation, moving boundary problems, phase transformations, 3D problems requiring remeshing, and nonlinear thermal analysis [1] are areas in which the application of the FEM is somehow limited. To overcome the aforementioned difficulties, meshless methods have been introduced and developed during the past two decades. In the case of meshless methods, only a discrete set of nodes scattered through the problem domain and on the boundaries are used to approximate the fields associated with the problem. There is no need for element connectivity, the removal and addition of nodes to the domain are easily performed, and the obtained results are smooth. However, the computational cost of meshless methods is generally higher than that corresponding to the FEM. Consequently, any contribution made to the reduction of the computational cost for meshless methods can be regarded as an important progress.

According to the weak formulation used, there are two general classes of meshless methods. The first class is based on the global weak formulation. The element free Galerkin (EFG) method is the most established technique in this class. In the second class, a local weak formulation is used in which the meshless local Petrov–Galerkin (MLPG) method is the most widely employed technique.

Different meshless methods have been used for the analysis of linear and nonlinear heat transfer problems by some researchers [2–4]. Singh and coworkers were among the first ones who analyzed linear heat transfer problems by the element free Galerkin method [5–8]. The EFG method has also been used for the analysis of heat transfer in composites [9,10]. A. Singh and colleagues analyzed transient, nonlinear heat transfer problems in solids by the EFG method [1,11]. Divo and Kassab made use of meshless methods in the analysis of conjugate heat transfer problems [12,13]. Liu et al. used the MLPG for radiative heat transfer analysis [14–17]. Wang and coworkers proposed a meshless method for the analysis of transient heat conduction in FGMs [18]. Meshless methods have been also used for the inverse analysis of heat transfer problems [19–22]. Wu and Tao used MLPG for the analysis of heat conduction problem in irregular complex domains [23]. Zhang and Ouyang studied heat transfer due to viscous dissipation in molten polymer flow by employing the EFG method [24]. Zhang et al. [25] proposed the use of mass lumping in the EFG method for the analysis of transient heat conduction problems.

As mentioned previously, the computational cost of meshless methods is generally higher than that corresponding to other numerical methods. The accurate computation of domain integrals in meshless methods based on global weak form is one major reason for the high computational cost of such methods [26]. As a result, the fast and efficient computation of the domain integrals, especially in nonlinear transient problems, can significantly reduce the computational cost. Based on this idea and a previously established integration method [26], the authors have proposed a meshless technique for the analysis of nonlinear transient heat transfer problems in FGMs in the presence of non-homogenous and/or temperature dependent heat sources. Mohammadi et al. [27] presented a somewhat similar method for the boundary element (BE) analysis of transient nonlinear heat conduction problems. Although their method is a robust technique for the accurate analysis of complex heat conduction problems, its application is confined to homogeneous media only. Actually, since the fundamental solutions for non-homogenous materials are in general not available, the boundary element method (BEM) cannot be easily used for the analysis of physical phenomena in such materials.

Most of the presented meshless studies related to heat conduction are performed by the EFG and MLPG methods and there is no use of the meshless radial point interpolation method (RPIM) for the heat conduction problems. In this paper, the RPIM along with the mentioned integration method have been employed for the analysis of nonlinear transient heat conduction problems. Since the shape functions used in the RPIM possess the Kronecker delta function property, the imposition of the essential boundary conditions is efficiently performed as in the FEM. In the original RPIM, the domain integrals in the weak formulation of the problem are evaluated by the use of a so-called background mesh and the Gaussian quadrature method. The accurate computation of the domain integrals by this method, especially in domains with complex geometry, is a time consuming task. As a result, the efficient computation of such domain integrals can significantly reduce the computational effort, especially when the domain integrals are to be evaluated repeatedly, as in the nonlinear transient problems. It should also be mentioned that the use of the background mesh for the evaluation of domain integrals diminishes the main advantage of meshless methods. Based on the mentioned facts, the method to be proposed here not only benefits from high accuracy and efficiency, but also is truly meshless.

Some problems involving various types of heat sources are analyzed in order to show the efficiency of the proposed method. The convergence of the proposed method with respect to the time step size and number of nodes and integration point is also studied.

2. An improved meshless radial point interpolation formulation of general nonlinear heat conduction problem

Since the early proposal of the meshless RPIM [28], various versions of the method for the analysis of various types of engineering problems have been introduced by several researchers. The RPIM has been used with global as well as local weak formulations [29]. The method, in conjunction with the boundary integral equation technique, has proven to be efficient in the analysis of engineering problems [30,31]. In the meshless RPIM, radial and polynomial basis functions are used for the construction of the shape functions. It is not necessary to use polynomial basis functions in the formulation of RPIM shape functions. However, studies show that when only the radial basis functions (RBF) are used for the construction of shape functions, the standard patch tests cannot be passed [32]. Adding the polynomial basis functions of any order, ensures completeness of the shape functions to that order. For instance, addition of polynomial basis functions up to linear order ensures C^1 consistency. The RPIM shape functions usually possess high order of continuity, because the RBFs can be easily selected to have the desired order of continuity. The shape functions in the RPIM possess the Kronecker delta function property; therefore, in the methods that use the RPIM shape functions for the approximation of the field function, the essential boundary conditions are imposed directly. Partition of unity is another feature of the RPIM shape functions.

When a local weak form is used with the RPIM shape functions, the resulting method is truly meshless, i.e. the local RPIM [32], the main reason for this being represented by the fact that integrations are performed over small sub-domains; consequently, a global background mesh is not necessary. Nonetheless, when the global weak form is used, the integrals are performed over the entire problem domain and if a background mesh is used to perform these integrations then the resulting method is not truly meshless. Here, we present an improved global meshless RPIM which benefits from a meshless integration technique, and therefore is truly meshless.

2.1. The numerical formulation

The RPIM interpolation augmented with polynomials can be used to obtain an approximation $T^h(\mathbf{x}, t)$ for the temperature function $T(\mathbf{x}, t)$:

$$T^h(\mathbf{x},t) = \sum_{i=1}^{n} R_i(\mathbf{x})a_i(t) + \sum_{j=1}^{m} p_j(\mathbf{x})b_j(t) = \mathbf{R}^T(\mathbf{x})\mathbf{a}(t) + \mathbf{p}^T(\mathbf{x})\mathbf{b}(t), \tag{1}$$

where R_i is a radial basis function, p_j is a monomial in spatial coordinates, n is the number of nodes in the support domain of the point $\mathbf{x}$, m is the number of polynomial basis functions, and a_i and b_j are time dependent unknown coefficients to be determined. In the present study, only linear monomials are used, i.e. $m = 3$. The value of n will be obtained based on the support domain size, which will be addressed later.

The independent variable in the radial basis functions is the Euclidean distance between the point $\mathbf{x}$ and a node at $\mathbf{x}_i$. The vectors $\mathbf{R}(\mathbf{x})$ and $\mathbf{p}(\mathbf{x})$ in Eq. (1) are defined as follows:

$$\mathbf{R}^T = [R_1(\mathbf{x})R_2(\mathbf{x})\cdots R_n(\mathbf{x})], \tag{2-a}$$

$$\mathbf{p}^T = [p_1(\mathbf{x})p_2(\mathbf{x})\cdots p_m(\mathbf{x})]. \tag{2-b}$$

There are some specific radial basis functions used in the meshless RPIM. Four frequently used RBFs are the multi-quadrics (MQ) function, the Gaussian (Exp) function, the thin plate Spline (TPS) function, and the Logarithmic radial basis function. The expression for each of the mentioned functions is given in Table 1. In the present work, the TPS functions are used for the construction of shape functions.

α_c, q, and η in the expression of the RBFs in Table 1 are shape parameters that should be carefully selected. d_c is the average nodal spacing in the support domain. In order to obtain well-conditioned moment matrices in the evaluation of the TPS shape functions, Liu and Gu [32] suggest to set η equal to either of the following values: 4.001, 5.001, or 6.001. In the present study, the value used for η is 4.001.

The $n + m$ unknown coefficients in Eq. (1) can be found by imposing the Kronecker delta function property and some specific constraint equations. The constraint equations are necessary to ensure that the coefficients are obtained uniquely [33]. These constraints can be expressed as follows:

$$\sum_{i=1}^{n} p_j(\mathbf{x}_i)a_i(t) = \mathbf{P}_m^T\mathbf{a} = 0, \quad j = 1, 2, \cdots, m, \tag{3}$$

Table 1
Conventional RBFs used in the RPIM.

Type	Expression
Multi-quadrics (MQ)	$R_i = (r_i^2 + (\alpha_c d_c)^2)^q$
Gaussian (EXP)	$R_i = \exp\left(-\alpha_c\left(\frac{r_i}{d_c}\right)^2\right)$
Thin plate Spline (TPS)	$R_i = r_i^\eta$
Logarithmic	$R_i = r_i^\eta \log(r_i)$

where:

$$\mathbf{P}_m^{\mathbf{T}} = \begin{bmatrix} 1 & 1 & \cdots & 1 \\ x_1 & x_2 & \cdots & x_n \\ y_1 & y_2 & \cdots & y_n \\ z_1 & z_2 & & z_n \\ \vdots & \vdots & \ddots & \vdots \\ p_m(\mathbf{x}_1) & p_m(\mathbf{x}_2) & \cdots & p_m(\mathbf{x}_n) \end{bmatrix}. \tag{4}$$

In this way the approximation function can be written as:

$$T^h(\mathbf{x},t) = \sum_{i=1}^{n} \phi_i(\mathbf{x})T_i(t) = \mathbf{\Phi}^{\mathbf{T}}(\mathbf{x})\mathbf{T}(t), \tag{5}$$

where **T** is a vector containing the nodal values of the temperature, and $\mathbf{\Phi}$ is a vector containing the first n components of the following vector:

$$\tilde{\mathbf{\Phi}} = \begin{bmatrix} \mathbf{R}^T & \mathbf{p}^T \end{bmatrix} \mathbf{G}^{-1}. \tag{6}$$

In Eq. (6), **G** is the so-called moment matrix and is obtained as follows:

$$\mathbf{G} = \begin{bmatrix} \mathbf{R}_0 & \mathbf{P}_m \\ \mathbf{P}_m^T & \mathbf{0} \end{bmatrix},$$

$$\mathbf{R}_0 = \begin{bmatrix} R_1(r_1) & R_2(r_1) & \cdots & R_n(r_1) \\ R_1(r_2) & R_2(r_2) & \cdots & R_n(r_2) \\ \vdots & \vdots & \cdots & \vdots \\ R_1(r_n) & R_2(r_n) & \cdots & R_n(r_n) \end{bmatrix}, \tag{7}$$

where r_k in the formulation of $R_i(r_k)$ is defined as follows:

$$r_k = \sqrt{(x_k - x_i)^2 + (y_k - y_i)^2 + (z_k - z_i)^2}. \tag{8}$$

The accuracy of the interpolation at each point, among other factors, is dependent on the shape and size of the support domain. In this work, the simple, yet effective, method of Liu and Gu [32] is used to determine the dimensions of the support domain. In this method, the dimension of the support domain is determined by $d_s = \alpha_s d_c$, where α_s is a constant, usually around 1.5, and d_c is the average nodal spacing in the support domain. A simple relation for obtaining the average nodal spacing is given by Liu and Gu [32]. Herein the shape of support domain is circular and spherical in 2D and 3D problems, respectively.

Consider now the general transient heat conduction equation for an isotropic medium:

$$\nabla \cdot (k(\mathbf{x},T)\nabla T(\mathbf{x},t)) + g(\mathbf{x},T,t) = \rho(\mathbf{x},T)c(\mathbf{x},T)\frac{\partial T(\mathbf{x},t)}{\partial t}, \tag{9}$$

where ρ is the density, c is the specific heat, k is the thermal conductivity, and g is the heat generation per unit volume. The initial and boundary condition for Eq. (9) are as follows:

$T(\mathbf{x},0) = T_0(\mathbf{x})$ in the domain (Ω),
$T = \overline{T}$ on the boundaries with the essential condition (Γ_1),
$-k(\nabla T \cdot \mathbf{n}) = \bar{q}$ on the boundaries with the natural condition (Γ_2),

where **n** is the unit outward normal vector to the boundary, T_0 is the initial condition, $\overline{T}$ is the applied temperature on the boundary, and $\bar{q}$ is the applied normal heat flux through the boundary.

On using Eq. (5) in the Galerkin weak form of Eq. (9), one obtains the following system of equations:

$$\mathbf{M}(T)\dot{\mathbf{T}} + \mathbf{K}(T)\mathbf{T} = \mathbf{F}(T,t), \tag{10}$$

where:

$$M_{ij} = \int_\Omega \rho(\mathbf{x},T)c(\mathbf{x},T)\phi_i\phi_j\, d\Omega, \tag{11}$$

$$K_{ij} = \int_\Omega k(\mathbf{x},T)\left[\frac{\partial\phi_i}{\partial x}\frac{\partial\phi_j}{\partial x} + \frac{\partial\phi_i}{\partial y}\frac{\partial\phi_j}{\partial y} + \frac{\partial\phi_i}{\partial z}\frac{\partial\phi_j}{\partial z}\right] d\Omega, \tag{12}$$

$$F_i = \int_\Omega g(\mathbf{x},T,t)\phi_i d\Omega - \int_{\Gamma_2} \bar{q}\phi_i\, d\Gamma. \tag{13}$$

After applying the Crank–Nicholson time integration scheme [34] to Eq. (10), one can write the equilibrium equation for the $(s+1)$ th time step as follows:

$$\hat{\mathbf{K}}_{s+1}\mathbf{T}_{s+1} = \overline{\mathbf{K}}_s\mathbf{T}_s + \hat{\mathbf{F}}_{s,s+1}, \tag{14}$$

$$\hat{\mathbf{K}}_{s+1} = \mathbf{M}_{s+1} + \frac{1}{2}\Delta t_{s+1}\mathbf{K}_{s+1}, \tag{15}$$

$$\overline{\mathbf{K}}_s = \mathbf{M}_s - \frac{1}{2}\Delta t_{s+1}\mathbf{K}_s, \tag{16}$$

$$\hat{\mathbf{F}}_{s,s+1} = \frac{1}{2}\Delta t_{s+1}[\mathbf{F}_{s+1} + \mathbf{F}_s]. \tag{17}$$

In Eqs. (14)–(17), the subscript indicates the time step number. Since in the most general case, the thermal properties of the material, and also the heat source vary with respect to the temperature, the problem solution at each time step should be iterative. The mass and stiffness matrices and the load vector at each time step are computed using the temperature distribution at the previous time step. Afterwards, these matrices and the load vector are updated iteratively at each time step until the solution converges to the desired accuracy.

2.2. The Cartesian transformation method for the evaluation of domain integrals

From Eqs. (11)–(13) it is clear that at each iteration corresponding to every time step of the analysis, some domain integrals should be evaluated. Therefore, a large number of domain integrals should be evaluated during the entire analysis. Consequently, the fast and efficient computation of these integrals affects the overall efficiency of the method. In this section, the 2D Cartesian transformation method (CTM) [26] with a modification is presented. This method is specially designed for situations in which a large number of domain integrals with different integrands should be evaluated in a single domain.

Consider a regular integral over a 2D domain (see also Fig. 1):

$$I = \int_{\Omega} h(\mathbf{x})\,d\Omega. \tag{18}$$

In order to obtain a meshless integration technique, the domain integral is first transformed into a boundary and a 1D integral as follows [35,36]:

$$I = \int_{\Gamma}\int_{a}^{x} h(\xi, y)\,d\xi dy. \tag{19}$$

By considering a rectangular auxiliary domain that encircles the original domain, the integral in Eq. (19) can be further transformed into two 1D integrals [26]:

$$I = \int_{Y_1}^{Y_2} g(y)\,dy, \tag{20}$$

where

$$g(y) = \int_{a}^{b} h(x,y)\,dx. \tag{21}$$

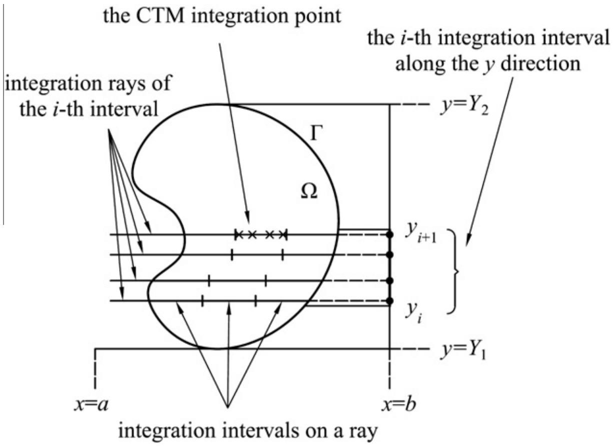

Fig. 1. An integration domain in 2D and its boundary.

The 1D integrals in Eqs. (20) and (21) can be evaluated by any numerical integration method, such as the composite Gaussian quadrature to give [26], (see Fig. 1):

$$I = \sum_{i=1}^{u} \sum_{j=1}^{v} J w_j G(\eta_j), \tag{22}$$

where $G(\eta) = g(y(\eta))$ and $J = dy/d\eta = (y_{i+1} - y_i)/2$; $g(y_i)$ is evaluated according to the following relation:

$$g(y_i) = \sum_{j=1}^{l} \left(\int_{x_{2j-1}}^{x_{2j}} h(x, y_i)\, dx \right), \tag{23}$$

$$\int_{x_{2j-1}}^{x_{2j}} h(x, y_i)\, dx = \sum_{r=1}^{p} \sum_{s=1}^{q} J' w_s H(\zeta_s), \tag{24}$$

where $H(\zeta) = h(x(\zeta), y_i)$ and $J' = (x_{2j} - x_{2j-1})/2p$. The integration limits in Eq. (23) are obtained according to a procedure explained in [26].

After some straightforward manipulations, the integral in Eq. (18) can be written as [26]:

$$I = \sum_{i=1}^{N} W^{2D}(\mathbf{x}_i) \times h(\mathbf{x}_i) = \mathbf{w}^{2D} \cdot \mathbf{H}, \tag{25}$$

where $W^{2D}(\mathbf{x}_i)$ is the integration weight associated with the ith integration point located at $\mathbf{x}_i$, and N is the number of integration points associated with the CTM integration scheme. The three-dimensional counterpart of the 2D CTM, explained in this section, can be found in [26].

When the integrand in Eq. (18) is known at some scattered points over the domain only, a meshless interpolation scheme should be used for the evaluation of the integrand at the location of the integration points. This situation happens, for instance, when the domain integrals in Eqs. (11)–(13), corresponding to a nonlinear problem, should be evaluated. At each step of the problem solution when the nodal values of temperature are obtained, the value of the temperature at any integration point can be obtained by a matrix relation of the following form:

$$\{\mathbf{T}_{\text{int}}\}_{N\times 1} = [\mathbf{S}]_{N\times n} \{\mathbf{T}_{nodal}\}_{n\times 1}, \tag{26}$$

where $\mathbf{T}_{\text{int}}$ and $\mathbf{T}_{nodal}$ are vectors containing the temperature values at the integration points and nodes, respectively. Here N and n are the total numbers of integration points and nodes, respectively, over the entire domain. The matrix $\mathbf{S}$ is a sparse matrix whose elements are the interpolating shape functions. For example, the ith row of $\mathbf{S}$ contains the shape functions of the nodes that are located in the support domain of the ith integration point. The matrix is sparse because only a small number of nodes are located in the support domain of each integration point. This matrix has the following form:

$$\mathbf{S} = \begin{bmatrix} \phi_1(\mathbf{x}_1) & \phi_2(\mathbf{x}_1) & \cdots & \phi_n(\mathbf{x}_1) \\ \phi_1(\mathbf{x}_2) & \phi_2(\mathbf{x}_2) & \cdots & \phi_n(\mathbf{x}_2) \\ \vdots & \vdots & \ddots & \vdots \\ \phi_1(\mathbf{x}_N) & \phi_2(\mathbf{x}_N) & \cdots & \phi_n(\mathbf{x}_N) \end{bmatrix}. \tag{27}$$

If the problem geometry does not change during the problem solution, the matrix $\mathbf{S}$ in Eq. (26) and the vector $\mathbf{w}^{2D}$ in Eq. (25) need only be evaluated once. In this way, the evaluation of the domain integrals at each time step reduces to simple vector and matrix multiplications. Since it has been shown that the CTM improves the accuracy of the meshless RPIM method [26], the use of the proposed technique for the evaluation of the domain integrals in transient nonlinear heat transfer problems not only enhances the accuracy, but also can decrease the overall computational cost of the calculations.

At each step of the problem solution, for the evaluation of the domain integrals in Eqs. (11)–(13) by the CTM, the following relations are used:

$$M_{ij} = \sum_{l=1}^{N} W_l^{2D} (R_l \times C_l \times S_{i,l} \times S_{j,l}), \tag{28}$$

$$K_{ij} = \sum_{l=1}^{N} W_l^{2D} [A_l (S_{i,l}^x \times S_{j,l}^x + S_{i,l}^y \times S_{j,l}^y)], \tag{29}$$

$$F_i = \sum_{l=1}^{N} W_l^{2D} (G_l \times S_{i,l}), \tag{30}$$

where $S_{i,l}$ is the lth element of the ith row of the matrix $\mathbf{S}$, in Eq. (27), and:

$$\{\mathbf{R}\} = \begin{Bmatrix} \rho(\mathbf{x}_1, T) \\ \rho(\mathbf{x}_2, T) \\ \vdots \\ \rho(\mathbf{x}_N, T) \end{Bmatrix}; \quad \{\mathbf{C}\} = \begin{Bmatrix} c(\mathbf{x}_1, T) \\ c(\mathbf{x}_2, T) \\ \vdots \\ c(\mathbf{x}_N, T) \end{Bmatrix}; \quad \{\mathbf{A}\} = \begin{Bmatrix} k(\mathbf{x}_1, T) \\ k(\mathbf{x}_2, T) \\ \vdots \\ k(\mathbf{x}_N, T) \end{Bmatrix}, \tag{31-a}$$

$$\{\mathbf{G}\} = \begin{Bmatrix} g(\mathbf{x}_1, T, t) \\ g(\mathbf{x}_2, T, t) \\ \vdots \\ g(\mathbf{x}_N, T, t) \end{Bmatrix}, \tag{31-b}$$

$$[S^x] = \begin{bmatrix} \frac{\partial\phi_1(\mathbf{x}_1)}{\partial x} & \frac{\partial\phi_2(\mathbf{x}_1)}{\partial x} & \cdots & \frac{\partial\phi_n(\mathbf{x}_1)}{\partial x} \\ \frac{\partial\phi_1(\mathbf{x}_2)}{\partial x} & \frac{\partial\phi_2(\mathbf{x}_2)}{\partial x} & \cdots & \frac{\partial\phi_n(\mathbf{x}_2)}{\partial x} \\ \vdots & \vdots & \ddots & \vdots \\ \frac{\partial\phi_1(\mathbf{x}_N)}{\partial x} & \frac{\partial\phi_2(\mathbf{x}_N)}{\partial x} & \cdots & \frac{\partial\phi_n(\mathbf{x}_N)}{\partial x} \end{bmatrix}, \tag{31-c}$$

$$[S^y] = \begin{bmatrix} \frac{\partial\phi_1(\mathbf{x}_1)}{\partial y} & \frac{\partial\phi_2(\mathbf{x}_1)}{\partial y} & \cdots & \frac{\partial\phi_n(\mathbf{x}_1)}{\partial y} \\ \frac{\partial\phi_1(\mathbf{x}_2)}{\partial y} & \frac{\partial\phi_2(\mathbf{x}_2)}{\partial y} & \cdots & \frac{\partial\phi_n(\mathbf{x}_2)}{\partial y} \\ \vdots & \vdots & \ddots & \vdots \\ \frac{\partial\phi_1(\mathbf{x}_N)}{\partial y} & \frac{\partial\phi_2(\mathbf{x}_N)}{\partial y} & \cdots & \frac{\partial\phi_n(\mathbf{x}_N)}{\partial y} \end{bmatrix}. \tag{31-d}$$

It should be noted that since the problem domain and the nodal arrangement do not change during the analysis, the matrices containing the shape functions and their derivatives, Eqs. (27), (31-c), and (31-d) remain constant during the analysis. Therefore, these matrices are evaluated and saved once in the first step, and they are used in the subsequent steps.

According to our experience, it is concluded that only the total number of nodes governs the necessary number of integration points required for accurate computations. Neither the number of nodes in the support domain of integration points, nor the order of polynomial basis functions has an important effect on the optimum number of integration points required for a precise integration. Our investigations show that, in order to obtain accurate results from the integration method described, the average nodal spacing of the proposed meshless method should be about 1.5–2.5 times the average spacing of the integration points for 2D problems. This ratio suffices to be in the range 2.0–2.5 for 3D problems. This point is observed when the four-point Gaussian quadrature is used for calculating the integrations in Eqs. (22) and (24). For obtaining the average spacing of the nodes and integration points, the method explained for determining the nodal spacing in a support domain is used. To be more specific, an average nodal spacing near each node is calculated; the average spacing value of all nodes is then evaluated and used as the average nodal spacing of all nodes. It should be mentioned that one can use larger number of integration points than the values stated above; nevertheless, the improvement in the accuracy is negligible.

3. Numerical results and discussion

In this section, two transient nonlinear heat conduction problems under the application of different heat generation sources are studied. The meshless RPIM and the numerical integration method presented in this paper are used for the analysis of the problem. In each case, with different heat generation, the convergence of the method with respect to the number of nodes and also the time step size is studied. Furthermore, the numerical results obtained, are compared with those of the FEM (ANSYS). The numerical analysis of the following examples was carried out using MATLAB codes run on a PC system with an Intel (R) Core™ 2 Quad CPU Q9550 @ 2.83 GHz and 4.00 GB of RAM.

3.1. Example 1: A 2D transient nonlinear problem

The problem geometry, boundary, and initial conditions are depicted in Fig. 2(a). An FGM made of zirconium oxide (ZrO_2) and titanium alloy (Ti–6Al–4 V) is considered. The thermal properties of the constituent materials are temperature dependent and for the temperature range of $300K \leqslant T \leqslant 1100$ K these are given as follows [37]:

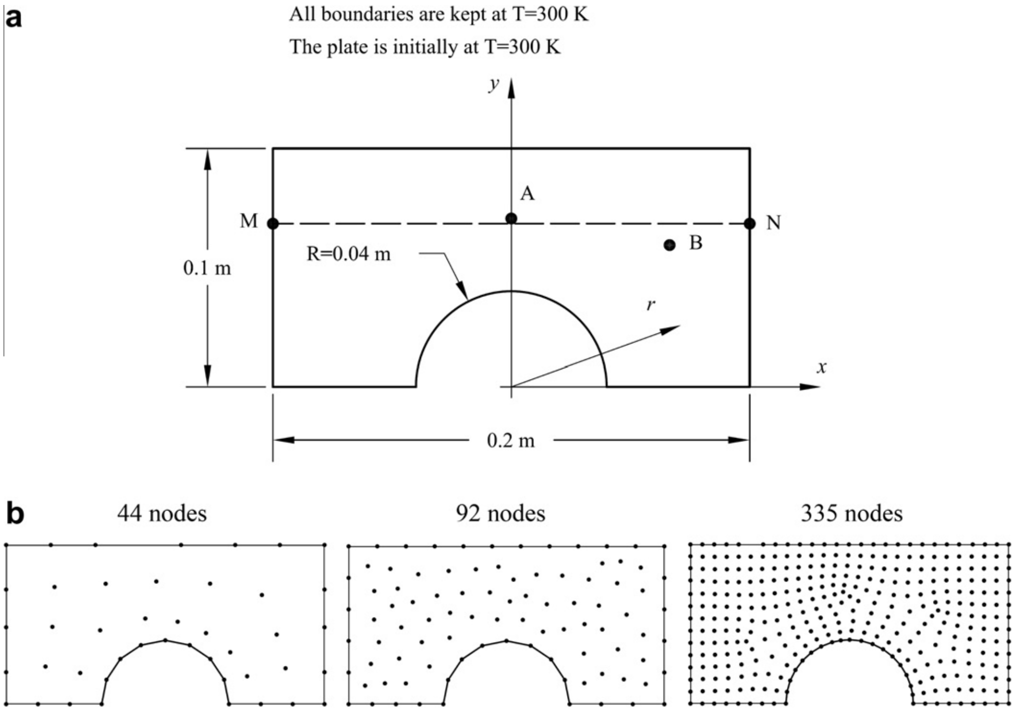

Fig. 2. Configuration of the problem, example 1: (a) the geometry and initial/boundary conditions and (b) node arrangements.

Material 1 (ZrO_2):

$$\begin{aligned} k &= 1.71 + 2.1 \times 10^{-4} T + 1.16 \times 10^{-7} T^2 \ [\mathrm{W/(mK)}], \\ c &= 2.74 \times 10^{2} + 7.95 \times 10^{-1} T - 6.19 \times 10^{-4} T^2 + 1.71 \times 10^{-7} T^3 \ [\mathrm{J/(kgK)}], \\ \alpha &= 1.331 \times 10^{-5} - 1.89 \times 10^{-8} T + 1.27 \times 10^{-11} T^2 \ [1/\mathrm{K}], \\ \rho &= 3657/[1 + \alpha(T - 300)]^3 \ [\mathrm{kg/m^3}]. \end{aligned} \tag{32}$$

Material 2 (Ti–6Al–4 V):

$$\begin{aligned} k &= 1.1 + 1.7 \times 10^{-2} T \ [\mathrm{W/(mK)}], \\ c &= 3.5 \times 10^{2} + 8.78 \times 10^{-1} T - 9.74 \times 10^{-4} T^2 + 4.43 \times 10^{-7} T^3 \ [\mathrm{J/(kgK)}], \\ \alpha &= 7.43 \times 10^{-6} + 5.56 \times 10^{-9} T - 2.69 \times 10^{-12} T^2 \ [1/\mathrm{K}], \\ \rho &= 4420/[1 + \alpha(T - 300)]^3 \ [\mathrm{kg/m^3}]. \end{aligned} \tag{33}$$

It is assumed that the volume fraction of each constituent of the FGM varies linearly with the radial distance, from Ti–6Al–4 V to ZrO_2 (see Fig. 2(a)). There are several models to evaluate effective properties of FGMs. The main emphasis of this work is on the heat conduction analysis rather than on modeling, therefore each effective property of the FGM at a point is evaluated by the simple mixture rule [38] as follows:

$$p = p_1 v_1 + p_2 v_2, \tag{34}$$

where v_1 and v_2 are the volume fractions of the materials 1 and 2, respectively, and p_1 and p_2 are the corresponding values of the property for each material. The following functions are considered for the volume fractions:

$$v_1 = \frac{r - R}{R' - R}, \quad v_2 = 1 - v_1, \tag{35}$$

where, according to Fig. 2(a), $R = 0.04$ and $R' = 0.1\sqrt{2}$.

Three different node arrangements are considered for the convergence study of the meshless RPIM. Fig. 2(b) depicts the node arrangements and also the number of nods in each case. The average nodal spacing for the arrangements with 335, 92, and 44 nodes is 0.009, 0.021, and 0.036, respectively. The FEM mesh used in ANSYS is shown in Fig. 3. 3871 quadrilateral four-node elements with 3995 nodes are used in the FEM mesh.

For the evaluation of the domain integrals, the four-point Gaussian quadrature method is used in each integration interval of the CTM. Also, in each case the number of integration points is chosen in such a manner that the average spacing of the nodes is twice that of the integration points.

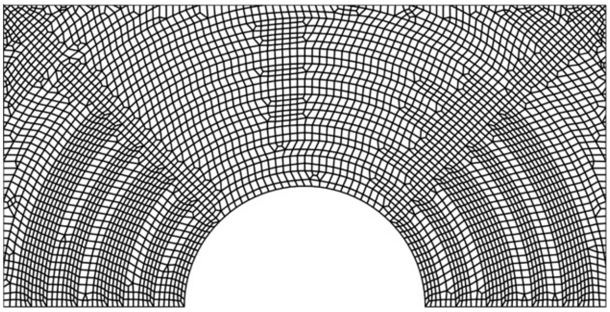

Fig. 3. The finite element mesh, 3871 elements and 3995 nodes.

Three different cases are analyzed by the meshless RPIM and also ANSYS. In the first case, the heat generation source varies with the spatial coordinates, but is constant with respect to time and the body temperature. In the second case, the heat generation source varies with the temperature, but is uniform over the body. In the third case, the heat generation source varies over the body and in time, but is independent of the body temperature.

In each case, two typical points in the body are selected for plotting the temperature variation with respect to time. One point is $A = [0, 0.7055]$ and the other one is $B = [0.0594, 0.0664]$. Also, the line MN, shown in Fig. 2(a), with $y = 0.0684$ is selected for the depiction of temperature variation within the body. In the first case, the effect of the total number of integration points of the CTM on the overall accuracy of the proposed meshless method is studied.

In the first case, the heat generation function in Eq. (9) is considered as follows:

$$g(x, y) = [1 + \sin(10\pi x)\sin(5\pi y)]5 \times 10^6. \tag{36}$$

As can be seen, the heat source has a sever variation over the domain.

Three different time step sizes of 15, 30, and 60 s are used for the analysis of the problem by the meshless RPIM. The temperature variation of the body along the line MN is shown in Fig. 4 for the three node arrangements of Fig. 2(b). It is clear that the proposed integration technique for the meshless RPIM has resulted in accurate results. In Fig. 4, the maximum relative error at $t = 180$ for the arrangements with 44, 92, and 335 nodes is 7.3%, 2.2%, and 0.2%, respectively.

Fig. 5 depicts the temperature variation along the line MN for different time step sizes. It is obvious that the proposed method has a small sensitivity to the time step size. The accuracy of the results obtained by the time step of 60 s is still acceptable. In Fig. 5, the maximum relative error at $t = 180$ for the time step sizes of 60, 30, and 15 s is 0.9%, 0.5%, and 0.2%, respectively.

The time history of the temperature at points A and B is plotted in Fig. 6. This figure clearly shows the excellent agreement between the results obtained by the proposed meshless method and those retrieved by using ANSYS with a fine mesh. Considering that the steady state temperature in the body takes place at around 600 s (Fig. 6), the time step size of 60 s is somewhat large. However, reasonably good results are obtained even with this time step size (see Fig. 5).

In order to study the effect of the number of integration points on the accuracy of the results, the temperature variation along the line MN is plotted for three different numbers of integration points in Fig. 7. In this figure, the ratios of the average

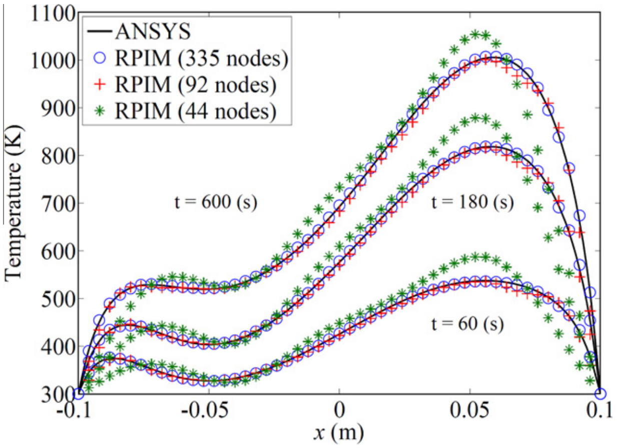

Fig. 4. Temperature variation along the line MN for different node arrangements and $\Delta t = 15$ s in case I.

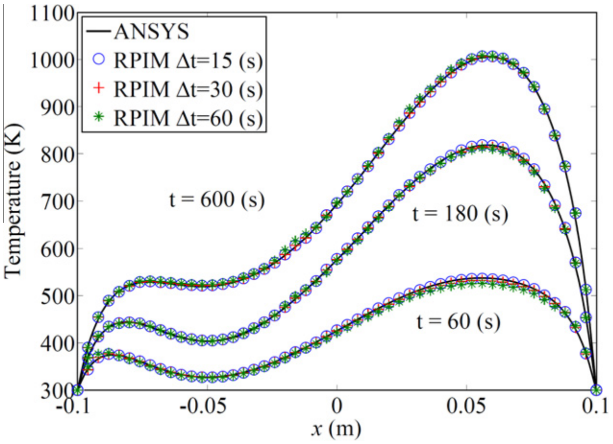

Fig. 5. Temperature variation along the line MN for different time steps and 335 nodes in case I.

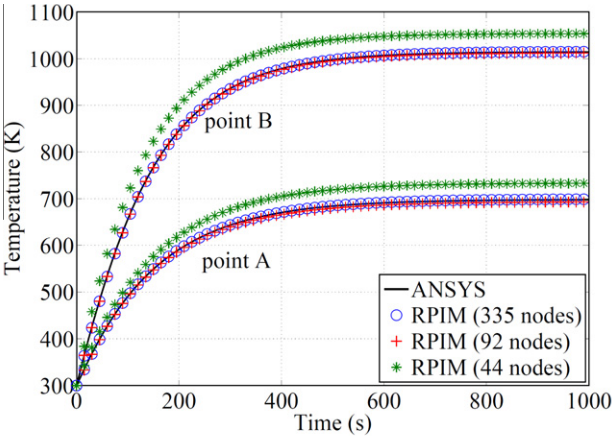

Fig. 6. Temporal temperature variation of points A and B for Δt = 15 s in case I.

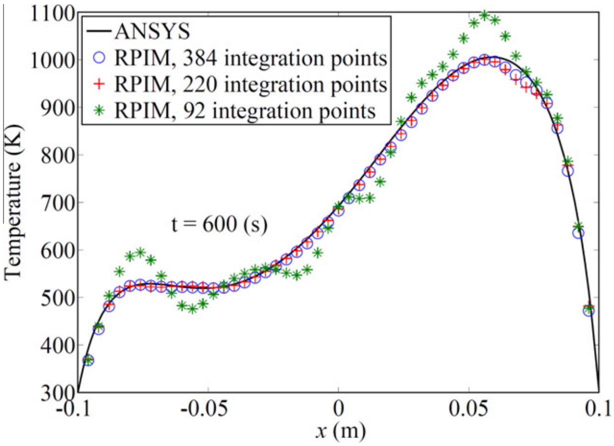

Fig. 7. Convergence of the proposed method with respect to the number of integration points, with 92 nodes and Δt = 15 s in case I.

spacing of nodes to the integration points of 1, 1.5, and 2 are selected for comparison of the results. These ratios correspond to 92, 220, and 384 integration points, respectively. The convergence of the proposed method with respect to the number of

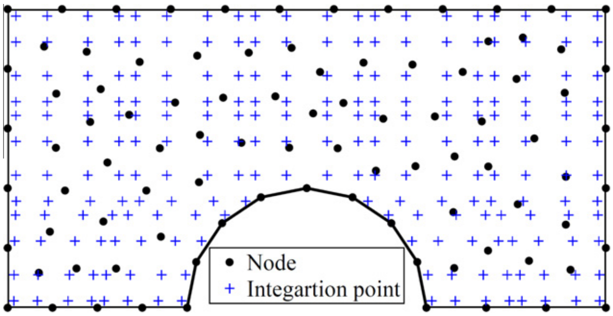

Fig. 8. Nodes and CTM integration points, for the arrangement with 92 nodes.

Table 2
CPU times (in s) for the analysis of example 1, case I.

	44 nodes			92 nodes			335 nodes		
	$N = 44$	$N = 112$	$N = 220$	$N = 92$	$N = 220$	$N = 384$	$N = 384$	$N = 768$	$N = 1360$
$\Delta t = 60(s)$	0.5	0.6	0.8	1.4	1.7	2.1	25	33	48
$\Delta t = 30(s)$	0.8	0.9	1.2	2.3	2.8	3.3	35	50	77
$\Delta t = 15(s)$	1.0	1.5	2.0	4.0	4.8	5.4	64	93	134

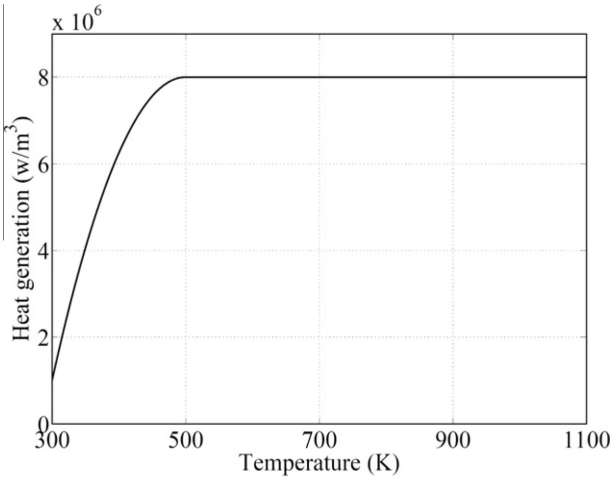

Fig. 9. Temperature variation of the heat generation source.

integration points is very good. In Fig. 7, the maximum relative error at $t = 600$ for the cases with 84, 220, and 384 integration points is 9.0%, 3.1%, and 1.9%, respectively.

Fig. 8 shows the integration points of the CTM in the problem domain. Also, the nodes of the meshless method are plotted. In this figure, the average spacing of the nodes is about 1.5 times that of the integration points.

The computational time consumption of the proposed improved RPIM is investigated for this case. For different combinations of the number of nodes, integration points, and time step size of the transient solution, the CPU time is given in Table 2. It should be pointed out that as the number of nodes and, consequently, the number of integration points is increased, the major computational time is due to the evaluation of domain integrals. Therefore, a computationally efficient meshless integration technique, as the one proposed in this study, can be very promising. In Table 2, N is the total number of integration points, and Δt is the time step size of the transient analysis.

In the second case, a temperature dependent heat source is considered. The variation of the heat source with respect to temperature is shown in Fig. 9. It can be clearly seen that the variation of the heat generation is quite sharp. As a result, the nonlinearity of the problem in this case is rather strong. The heat generation in this case has the following form:

$$g(x,y,T) = \begin{cases} 175T(10^3 - T) - 3.575 \times 10^7 & 300 \leqslant T \leqslant 500 \\ 8 \times 10^6 & T \geqslant 500 \end{cases}. \tag{37}$$

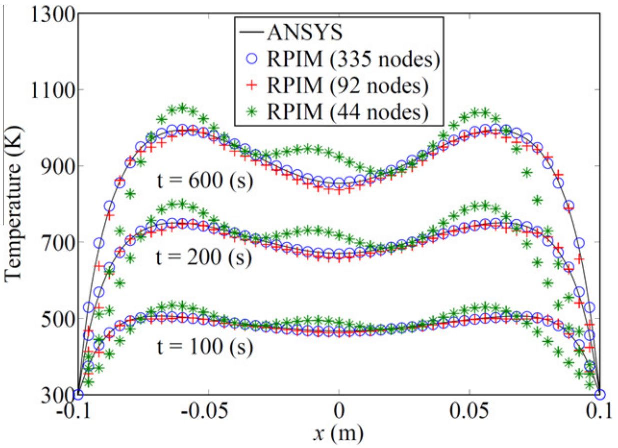

Fig. 10. Temperature variation along the line MN for different node arrangements and $\Delta t = 1$ s in case II.

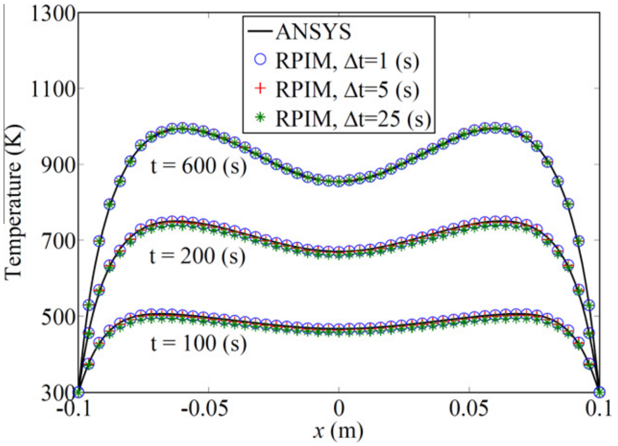

Fig. 11. Temperature variation along the line MN for different time steps and 335 nodes in case II.

The problem is analyzed with three different node arrangements (Fig. 2(b)) and three time step sizes of 1, 5, and 25 s. In Fig. 10, the temperature variation of the body along the line MN is plotted. In this figure the results obtained using the time step size of 1 s is reported. The good convergence of the proposed method with respect to the number of nodes is evident. In Fig. 10, the maximum relative error at $t = 200$ for the arrangements with 44, 92, and 335 nodes is 24.7%, 2.8%, and 0.2%, respectively.

Fig. 11 depicts the variation of temperature along the line MN with different time step sizes and 335 nodes. In Fig. 11, the maximum relative error at $t = 200$ for the time step sizes of 25, 5, and 1 s is 1.4%, 0.5%, and 0.2%, respectively.

The temperature variation of the points A and B with respect to time is plotted in Fig. 12. This figure clearly shows the excellent convergence of the proposed method. Noticing the large range of temperature variation during the time period of 600 s and the sharp variation of temperature near the boundaries (Figs. 10–12), we can conclude that the proposed meshless method has grasped the variation very well.

In the third case, a non-uniform and time-dependent, but temperature-independent heat source is considered. The heat source function considered in this case is expressed as follows:

$$
\begin{aligned}
& g(x,y,t) = [1+\sin(10\pi x)\sin(5\pi y)]5\times 10^{6}\times f(t) \\
& f(t) = \begin{cases} \frac{16}{3000}t\left(1-\frac{5}{3000}t\right)+0.2 & 0 \leqslant t \leqslant 300 \\ 1 & t \geqslant 300 \end{cases}
\end{aligned}
\tag{38}
$$

The function $f(t)$ in Eq. (38) is plotted in Fig. 13. For the analysis of the problem in this case, three node arrangements (Fig. 2(b)) and time step sizes of 1, 5, and 25 s are utilized. The variation of the temperature along the line MN is depicted in Fig. 14. The results presented in this figure correspond to the time step size of 1 s. Although the heat generation source

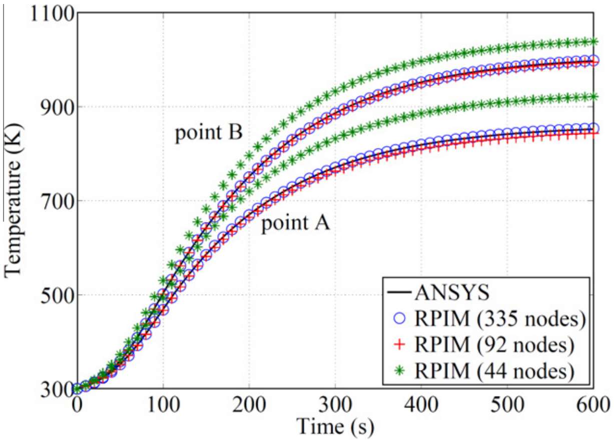

Fig. 12. Temporal temperature variation of points A and B for $\Delta t = 1$ s in case II.

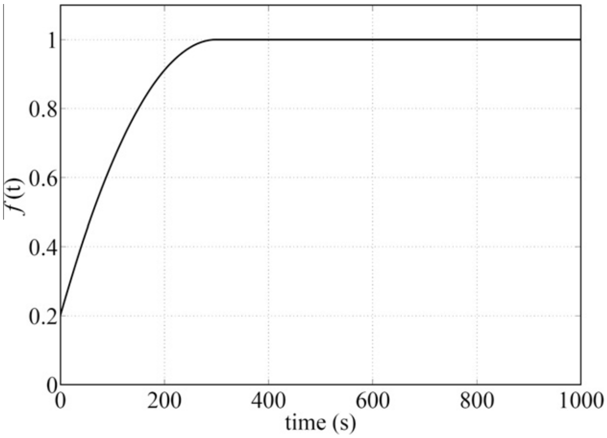

Fig. 13. The weight function of the heat generation source, case III.

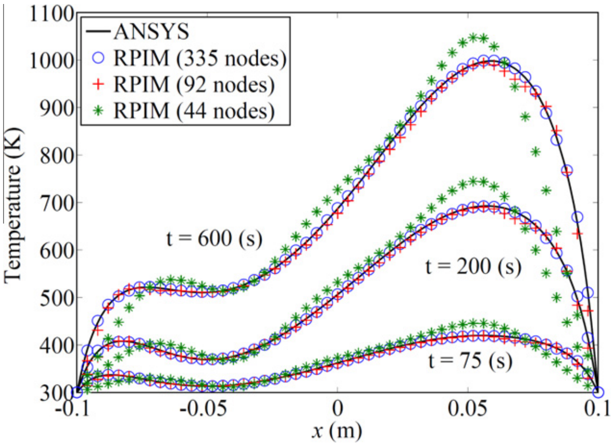

Fig. 14. Temperature variation along the line MN for different node arrangements and $\Delta t = 1$ s in case III.

varies sharply with time, the variation of the temperature is excellently predicted by the proposed method. In Fig. 14, the maximum relative error at $t = 200$ for the arrangements with 44, 92, and 335 nodes is 16.0%, 2.0%, and 0.1%, respectively.

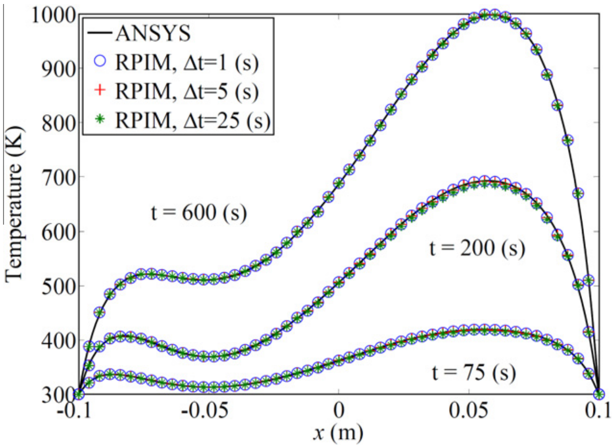

Fig. 15. Temperature variation along the line MN for different time steps and 335 nodes in case III.

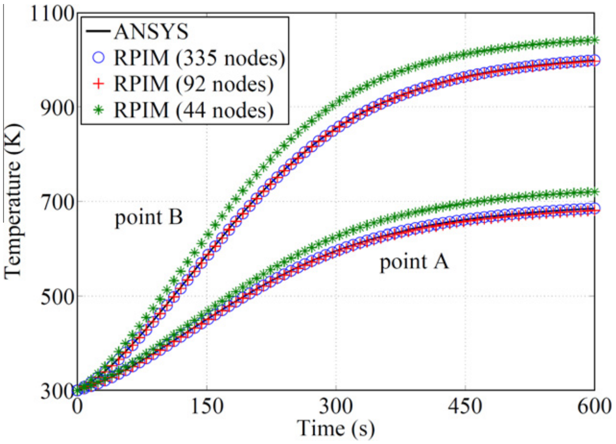

Fig. 16. Temporal temperature variation of points A and B for $\Delta t = 1$ s in case III.

Fig. 15 plots the temperature variation along the line MN, for the three different time step sizes mentioned above. The node arrangement with 335 nodes is used to obtain the results. As can be seen in Fig. 15, even the largest time step size generates accurate results although the source itself is time-varying. This means that with the present meshless method, transient heat conduction problems can be modeled with quite large time step sizes; this in turn, means that the method is very efficient for the analysis of transient nonlinear problems. In Fig. 15, the maximum relative error at $t = 200$ for the time step sizes of 25, 5, and 1 s is 1.0%, 0.3%, and 0.1%, respectively.

In Fig. 16 the time variation of the temperature at points A and B is shown. The results presented in this figure correspond to the time step size of 1 s. Convergence of the results is apparent.

3.2. Example 2: A 3D transient nonlinear problem

In this example, a quarter of a hollow cylinder made of a functionally graded material is considered. The material used in this example is the same as that from example 1. The cylinder includes a spatially variable heat source. Using the improved meshless RPIM developed in this paper, the transient temperature variation in the cylinder is obtained. The problem geometry, boundary, and initial conditions are described in Fig. 17(a).

Similar to the previous example, the effective properties of the FGM is evaluated by the mixture rule, Eq. (34), by taking $\upsilon_1 = 2r - 1$, $\upsilon_2 = 1 - \upsilon_1$, where r is the radial distance measured from the axis of the cylinder. The indices 1 and 2 refer to materials 1 and 2 in Eqs. (32) and (33), respectively. Three different node arrangements are considered for the convergence study of the meshless RPIM. Fig. 17(b) depicts the node arrangements and also the number of nodes used in each case. The average nodal spacing for the arrangements with 1815, 637, and 385 nodes is 0.132, 0.193, and 0.231, respectively. For

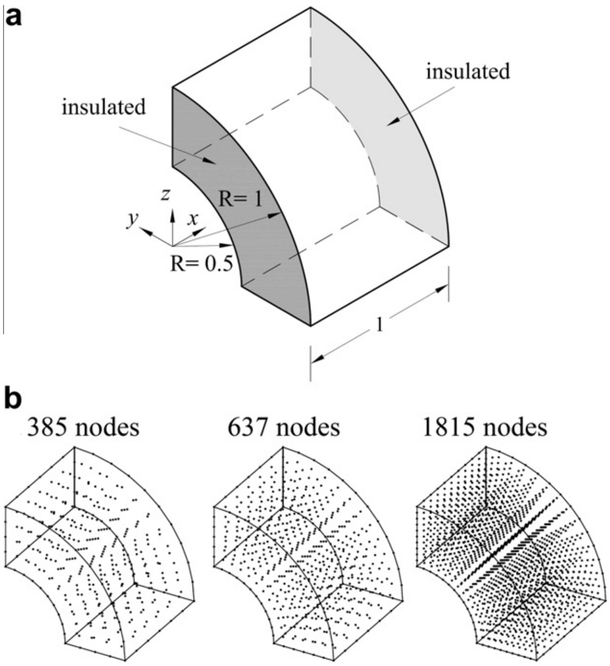

Fig. 17. Configuration of the problem, example 2: (a) the geometry; the body is initially at $T = 300$ K; all surfaces other than those indicated in the figure are kept at $T = 300$ K, (b) node arrangements.

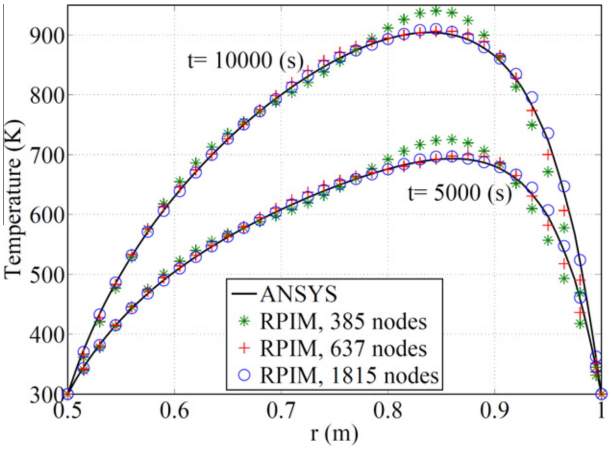

Fig. 18. Temperature variation along the radial line at $x = 0.5$ for different node arrangements and $\Delta t = 250$ s in example 2.

comparison purposes, the problem is also analyzed by ANSYS with a fine mesh (24000 eight-node brick elements and 26901 nodes).

A spatially variable heat source with the following equation is considered in the body:

$$g(x,y,z) = \left[y + (x^2 + y^2 + z^2)\cos\left(\frac{\pi}{2}x\right)\right]1.5 \times 10^5. \tag{39}$$

To validate the results obtained by the proposed method, two typical points in the body are selected for plotting the temperature variation with respect to time. These points are $A = (0.5;\ 0.4243;\ 0.4243)$ and $B = (0.5;\ 0.6187;\ 0.6187)$. Also, a radial line at $x = 0.5$ is selected for the depiction of temperature variation in the body. To study the convergence of the proposed method with respect to time step size, three different step sizes of 250, 500, and 1000 s are used for the analysis of the problem. The problem is analyzed in a time period of 10000 s.

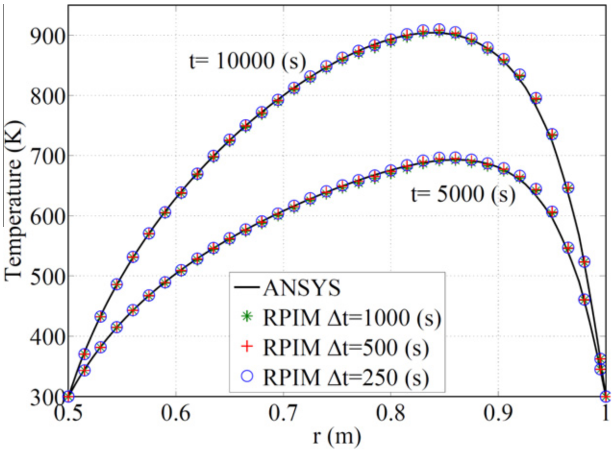

Fig. 19. Temperature variation along the radial line at $x = 0.5$ for different time steps and 1815 nodes in example 2.

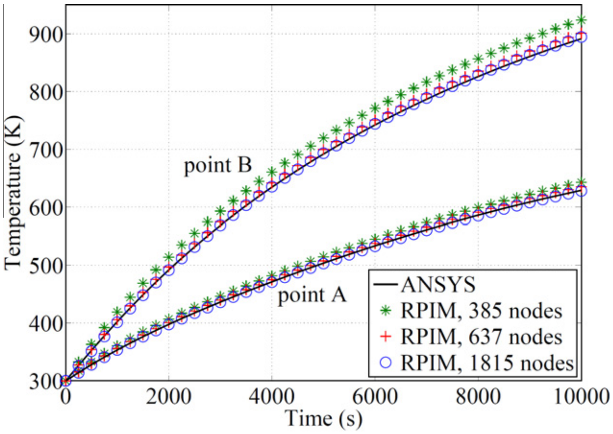

Fig. 20. Temporal temperature variation of points A and B for $\Delta t = 250$ s in example 2.

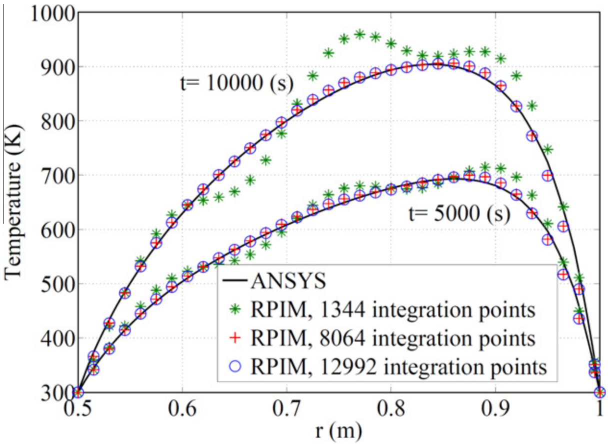

Fig. 21. Convergence of the proposed method with respect to the number of integration points, with 637 nodes and $\Delta t = 500$ s in example 2.

Table 3
CPU times (in s) for the analysis of example 2, with $\Delta t = 1000(s)$.

385 nodes		637 nodes		1815 nodes	
$N = 2176$	$N = 8064$	$N = 4240$	$N = 12992$	$N = 11760$	$N = 19072$
62	188	261	742	5025	7301

Fig. 18 presents the variation of temperature along the radial line at $x = 0.5$, for the three nodal arrangements considered. It is evident that the proposed method shows a good convergence with respect to the number of nodes. In Fig. 18, the maximum relative error at $t = 5000$ for the arrangement with 385, 637, and 1815 nodes is 8.5%, 3.9%, and 1.6%, respectively.

The temperature variation along the radial line at $x = 0.5$ is plotted in Fig. 19, with different time step sizes. The figure clearly shows the proposed method gives excellent results even with large time step sizes. In Fig. 19, the maximum relative error at $t = 5000$ for the time step size of 1000, 500, and 250 s is 2.7%, 2.0%, and 1.6%, respectively.

The time history of the temperature at points A and B is plotted in Fig. 20. This figure clearly shows the excellent agreement between the results obtained by the proposed meshless method and those retrieved by using ANSYS with a fine mesh.

In order to study the effect of the number of integration points on the accuracy of the results, the temperature variation along the radial line at $x = 0.5$ is also plotted for three different numbers of integration points in Fig. 21. In this figure, the ratios of the average spacing of nodes to the integration points of 1.3, 2.3, and 2.7 are selected for comparison of the results. These ratios correspond to 1344, 8064, and 12992 integration points, respectively. The convergence of the proposed method with respect to the number of integration points is obvious. In Fig. 21, the maximum relative error at $t = 10000$ for the case with 1344, 8064, and 12992 integration points is 10.4%, 1.9%, and 0.8%, respectively.

The computational time consumption of the proposed improved RPIM is investigated for this example as well. For various combinations of the number of nodes and integration points, the CPU time is given in Table 3. Again, in Table 3, N is the total number of integration points.

4. Conclusion

Based on a meshless integration technique, an improved meshless radial point interpolation method was presented. The proposed integration technique is capable of fast and accurate evaluation of domain integrals. The improved meshless RPIM presented in this paper has the advantage of being truly meshless, while having a better accuracy and computational efficiency in comparison with the original RPIM. Additionally, since the RPIM shape functions have the Kronecker delta function property, the enforcement of essential boundary conditions in the presented method is much simpler than in the case of the EFG and MLPG methods. The accuracy of the improved RPIM has been demonstrated through some 2D and 3D heat conduction problems. It was shown that the improved RPIM has an excellent performance for the prediction of the temperature distribution in nonlinear transient heat conduction problems. Also, the good convergence of the method with respect to the number of nodes and time step size has been verified. Moreover, it has been shown that for an accurate analysis, the average nodal spacing of the meshless method should be about 1.5–2.5 times the average spacing of the integration points for the 2D problems, and about 2.0–2.5 for 3D problems. This point was observed when the four-point Gaussian quadrature method is employed in integration intervals of the CTM.

References

[1] A. Singh, I.V. Singh, R. Prakash, Meshless element free Galerkin method for unsteady nonlinear heat transfer problems, Int. J. Heat Mass Transfer 50 (2007) 1212–1219.
[2] G. Demirkaya, C. Wafo Soh, O.J. Ilegbusi, Direct solution of Navier–Stokes equations by radial basis functions, Appl. Math. Model. 32 (2008) 1848–1858.
[3] L. Marin, Treatment of singularities in the method of fundamental solutions for two-dimensional Helmholtz-type equations, Appl. Math. Model. 34 (2010) 1615–1633.
[4] M. Shariyat, S.M.H. Lavasani, M. Khaghani, Nonlinear transient thermal stress and elastic wave propagation analyses of thick temperature-dependent FGM cylinders, using a second-order point-collocation method, Appl. Math. Model. 34 (2010) 898–918.
[5] I.V. Singh, K. Sandeep, R. Prakash, The element free Galerkin method in three-dimensional steady state heat conduction, Int. J. Comput. Eng. Sci. 3 (2002) 291–303.
[6] I.V. Singh, K. Sandeep, R. Prakash, Heat transfer analysis of two-dimensional fins using meshless element-free Galerkin method, Numer. Heat Transfer, Part A 44 (2003) 73–84.
[7] I.V. Singh, K. Sandeep, R. Prakash, Meshless EFG method in transient heat conduction problems, Int. J. Heat Technol. 21 (2003) 99–105.
[8] I.V. Singh, K. Sandeep, R. Prakash, Application of meshless element free Galerkin method in two-dimensional heat conduction problems, Comput. Assist. Mech. Eng. Sci. 11 (2004) 265–274.
[9] I.V. Singh, A numerical solution of composite heat transfer problems using meshless method, Int. J. Heat Mass Transfer 47 (2004) 2123–2138.
[10] I.V. Singh, M. Tanaka, Heat transfer analysis of composite slabs using meshless element free Galerkin method, Comput. Mech. 38 (2006) 521–532.
[11] A. Singh, I.V. Singh, R. Prakash, Meshless analysis of unsteady-state heat transfer in semi-infinite solid with temperature-dependent thermal conductivity, Int. J. Heat Mass Transfer 33 (2006) 231–239.
[12] E. Divo, A.J. Kassab, A meshless method for conjugate heat transfer problems, Eng. Anal. Bound. Elem. 29 (2005) 136–149.
[13] E. Divo, A.J. Kassab, Iterative domain decomposition meshless method modeling of incompressible viscous flows and conjugate heat transfer, Eng. Anal. Bound. Elem. 30 (2006) 465–478.
[14] L.H. Liu, Meshless method for radiation heat transfer in graded index medium, Int. J. Heat Mass Transfer 49 (2006) 219–229.

[15] L.H. Liu, J.Y. Tan, B.X. Li, Meshless approach for coupled radiative and conductive heat transfer in one-dimensional graded index medium, J. Quant. Spectrosc. Radiat. Transfer 101 (2006) 237–248.

[16] L.H. Liu, J.Y. Tan, Least-squares collocation meshless approach for radiative heat transfer in absorbing and scattering media, J. Quant. Spectrosc. Radiat. Transfer 103 (2007) 545–557.

[17] L.H. Liu, J.Y. Tan, Meshless local Petrov–Galerkin approach for coupled radiative and conductive heat transfer, Int. J. Therm. Sci. 46 (2007) 672–681.

[18] H. Wang, Q.-H. Qin, Y.-L. Kang, A meshless model for transient heat conduction in functionally graded materials, Comput. Mech. 38 (2006) 51–60.

[19] L. Marin, Numerical solution of the Cauchy problem for steady-state heat transfer in two-dimensional functionally graded materials, Int. J. Solids Struct. 42 (2005) 4338–4351.

[20] L. Marin, D. Lesnic, The method of fundamental solutions for nonlinear functionally graded materials, Int. J. Solids Struct. 44 (2007) 6878–6890.

[21] L. Marin, An alternating iterative MFS algorithm for the Cauchy problem in two-dimensional anisotropic heat conduction, CMC: Comput. Mater. Continua 12 (2009) 71–99.

[22] L. Yan, F.-L. Yang, C.-L. Fu, A meshless method for solving an inverse spacewise- dependent heat source problem, J. Comput. Phys. 228 (2009) 123–136.

[23] X.-H. Wu, W.-Q. Tao, Meshless method based on the local weak-forms for steady-state heat conduction problems, Int. J. Heat Mass Transfer 51 (2008) 3103–3112.

[24] X.-H. Zhang, J. Ouyang, Meshless analysis of heat transfer due to viscous dissipation in polymer flow, Eng. Anal. Bound. Elem. 32 (2008) 41–51.

[25] X.-H. Zhang, J. Ouyang, L. Zhang, Matrix free meshless method for transient heat conduction problems, Int. J. Heat Mass Transfer 52 (2009) 2161–2165.

[26] A. Khosravifard, M.R. Hematiyan, A new method for meshless integration in 2D and 3D Galerkin meshfree methods, Eng. Anal. Bound. Elem. 34 (2010) 30–40.

[27] M. Mohammadi, M.R. Hematiyan, L. Marin, Boundary element analysis of nonlinear transient heat conduction problems involving non-homogenous and nonlinear heat sources using time-dependent fundamental solutions, Eng. Anal. Bound. Elem. 34 (2010) 655–665.

[28] J.G. Wang, G.R. Liu, A point interpolation meshless method based on radial basis functions, Int. J. Numer. Methods Eng. 54 (2002) 1623–1648.

[29] G.R. Liu, L. Yan, J.G. Wang, Y.T. Gu, Point interpolation method based on local residual formulation using radial basis functions, Struct. Eng. Mech. 14 (2002) 713–732.

[30] G.R. Liu, Y.T. Gu, Boundary meshfree methods based on the boundary point interpolation methods, Eng. Anal. Bound. Elem. 28 (2004) 475–487.

[31] X. Li, J. Zhu, S. Zhang, A meshless method based on boundary integral equations and radial basis functions for biharmonic-type problems, Appl. Math. Model. 35 (2011) 737–751.

[32] G.R. Liu, Y.T. Gu, An Introduction to Meshfree Methods and their Programming, Springer, Netherlands, 2005. pp. 74–81.

[33] M.A. Golberg, C.S. Chen, H. Bowman, Some recent results and proposals for the use of radial basis functions in the BEM, Eng. Anal. Bound. Elem. 23 (1999) 285–296.

[34] J.N. Reddy, An Introduction to the Finite Element Method, second ed., McGraw-Hill, Singapore, 1993. pp. 227–230.

[35] M.R. Hematiyan, A general method for evaluation of 2D and 3D domain integrals without domain discretization and its application in BEM, Comput. Mech. 39 (2007) 509–520.

[36] M.R. Hematiyan, Exact transformation of a wide variety of domain integrals into boundary integrals in boundary element method, Commun. Numer. Methods Eng. 24 (2008) 1497–1521.

[37] Y.S. Touloukian, Thermophysical Properties of Matter, IFI/Plenum, New York, 1973. pp. 1272.

[38] G.R. Liu, X. Han, Computational Inverse Techniques in Nondestructive Evaluation, CRC, 2003. pp. 269–271.